The impact of climate change on ocean submesoscale activity

K.J. Richards,[1,2] D.B. Whitt,[3] G. Brett,[1] F.O. Bryan,[3] K. Feloy,[2] M.C. Long,[3]

K. J. Richards, International Pacific Research Center, University of Hawai'i at Mānoa, 1680 East West Road, Honolulu, HI 96822, USA. (rkelvin@hawaii.edu)

D.B. Whitt, National Center for Atmospheric Research, PO Box 3000, Boulder, CO, USA 80307. (dwhitt@ucar.edu)

G. Brett, International Pacific Research Center, University of Hawai'i at Mānoa, 1680 East West Road, Honolulu, HI 96822, USA. (brett33@hawaii.edu)

F.O. Bryan, National Center for Atmospheric Research, PO Box 3000, Boulder, CO, USA 80307. (bryan@ucar.edu)

K. Feloy, Department of Oceanography, University of Hawai'i at Mānoa, 1000 Pope Road, Honolulu, HI 96822, USA. (kfeloy@hawaii.edu)

M.C. Long, National Center for Atmospheric Research, PO Box 3000, Boulder, CO, USA 80307. (mclong@ucar.edu)

[1]International Pacific Research Center,

Abstract. Global warming may modify submesoscale activity in the ocean through changes in the mixed layer depth and lateral buoyancy gradients. As a case study we consider a region in the Northeast Atlantic under present and future climate conditions, using a time-slice method and global and nested regional ocean models. The high resolution regional model reproduces the strong seasonal cycle in submesoscale activity observed under present-day conditions. In the future, with a reduction in the mixed layer depth, there is a substantial reduction in submesoscale activity and an associated decrease in kinetic energy at the mesoscale. The vertical buoyancy flux induced by submesoscale activity is reduced by a factor of 2. When submesoscale activity is suppressed, by increasing the parameterized lateral mixing in the model, the climate change induces a larger reduction in winter mixed layer depths while there is less of a change in kinetic energy at the mesoscale. A scaling for the vertical buoyancy flux proposed by Fox-Kemper et. al. based on the

[1]University of Hawai'i at Mānoa, Honolulu, Hawaii, USA.

[2]Department of Oceanography, University of Hawai'i at Mānoa, Honolulu, Hawaii, USA.

[3]National Center for Atmospheric Research, Boulder, CO, USA.

properties of mixed layer instability (MLI), is found to capture much of the seasonal and future changes to the flux in terms of regional averages as well as the spatial structure, although it over predicts the reduction in the flux in the winter months. The vertical buoyancy flux when the mixed layer is relatively shallow is significantly greater than that given by the scaling based on MLI, suggesting during these times other processes (besides MLI) may dominate submesoscale buoyancy fluxes.

1. Introduction

The physical structure of the upper ocean is an important control on ocean-atmosphere exchange of momentum, heat, freshwater, and gases such as CO_2. It also regulates the distribution of nutrients and their delivery to the euphotic zone (the sunlit upper ocean), thereby impacting net primary productivity. Determining the mechanisms structuring upper ocean dynamics is critical to understanding how the physical climate system and biogeochemical cycles function. Moreover, we expect climate change to strongly impact these processes.

Important processes are associated with submesoscale motions, which have lateral scales of order 1–10 km and are characterized by sharp density gradients (fronts) and strong jets with large Rossby number. These dynamical features can induce very strong vertical motions [*Capet et al.*, 2008; *Klein and Lapeyre*, 2009; *McWilliams*, 2016] that impact the vertical flux of nutrients and biomass, which can both fuel and significantly damp primary production locally [*Lévy et al.*, 2001; *Lévy et al.*, 2012; *Mahadevan*, 2016; *Lévy et al.*, 2018]. A major source of the strong vertical motions at these scales is mixed layer baroclinic instabilities (MLI) [*Boccaletti et al.*, 2007; *Fox-Kemper et al.*, 2008]. In addition to the direct impacts of vertical motions on nutrient and biomass fluxes, the eddy-driven overturning streamfunction associated with submesoscale motions can lead to a restratification of the mixed layer [*Fox-Kemper et al.*, 2008] that can promote phytoplankton blooms by alleviating light limitation [*Taylor and Ferrari*, 2011; *Mahadevan et al.*, 2012]. From scaling arguments suggested by [*Fox-Kemper et al.*, 2008] (hereafter FFH) the strength of the overturning scales as $H^2|\nabla_h b|/|f|$, where H is the mixed layer

depth, $|\nabla_h b|$ is the cross-front horizontal buoyancy gradient and f is the Coriolis parameter. (The buoyancy, $b = -g\rho/\rho_0$ where g is the acceleration due to gravity, ρ density and ρ_0 a reference density.)

Because MLI may be a dominant process controlling the energetics of submesocales when mixed layers are sufficiently deep [*Callies et al.*, 2016], a useful indicator for submesoscale activity is the conversion rate of available potential energy, APE. On theoretical grounds, the APE conversion rate scales as $|\nabla_h b|^2 H^2/|f|$ (FFH). FFH test this scaling in an idealized flow regime while *Capet et al.* [2008] and *Mensa et al.* [2013] show it also holds in more realistic model flows of the Argentinian Shelf and Gulf Stream regions, respectively, although *Capet et al.* [2008] found the FFH scaling to underpredict the associated vertical buoyancy flux by a factor of 2-3. The dependence on H (the MLD) indicates the potential for strong seasonal modulation of submesoscale activity. Indeed, both *Capet et al.* [2008] and *Mensa et al.* [2013] find that submesoscale activity peaks in winter months when the mixed layer is deep. The role of variations in lateral density gradients in the seasonal variation of submesoscale activity varies regionally: the strength of lateral density gradients peaks with the depth of the mixed layer in the model Argentinian Shelf while this relationship does not hold for the model Gulf Stream region. *Sasaki et al.* [2014] also find a strong seasonality in submesoscale activity in a model of the North Pacific with it peaking in late winter when the mixed layer is at its deepest. Observational evidence of seasonality is growing. *Callies et al.* [2015] provide evidence based on *in situ* observations in the relatively energetic NW Atlantic of a strong enhancement of mixed-layer submesoscale activity during winter months. Seasonality in submesoscale activity is

also observed in the more quiescent parts of the North Pacific sub-tropical gyre [*Ascani et al.*, 2013] and the NE Atlantic [*Thompson et al.*, 2016].

Given this background, there is great potential for global warming to produce significant changes in ocean circulation dynamics at the submesoscale with unknown implications for the biogeochemistry and ecology of the upper ocean: an increase in the stratification of the near-surface ocean and decrease in mixed layer depth is expected to reduce submesoscale activity. In a complex system such as the ocean, the degree to which this conjecture holds true, or how important the processes may be, is not obvious. Whether changes in lateral buoyancy gradients, brought about by changes to eddy stirring for instance, will enhance or suppress MLIs is unclear. Furthermore, there will certainly be regional dependencies. Indeed, the analysis of CMIP3 models by *Capotondi et al.* [2012] shows regional variation in the projected change in upper ocean stratification during the second half of the 21st century relative to the second half of the 20th century, with the largest changes in the tropics, the Arctic, the North Atlantic and the northeast Pacific.

As a first step in evaluating the role of submesoscale processes in modulating the upper ocean response to climate change we present results from high-resolution nested regional simulations of the NE Atlantic. The simulation results are assessed in the context of extant theory for submesoscale mixed layer instability. The experimental design is described in Section 2. Results are presented in Section 3 with a focus on changes to horizontal wavenumber spectra and vertical buoyancy fluxes induced by global warming. Conclusions and closing discussion is given in Section 4.

2. Experimental design

2.1. Modeling Approach

Integrating a submesoscale resolving global model over a full climate-change scenario would be computationally expensive. Instead, we use a "time slice" approach, which makes use of several models and observations to generate submesoscale permitting solutions in a particular region and a "time slice" of interest (e.g., present day, nominally year 2000, or future climate, nominally at 2100).

Surface forcing with synoptic variability but without confounding inter-annual variability is obtained using the standard bulk flux algorithms of the Community Earth System Model (CESM) and the Coordinated Ocean-Ice Reference Experiment (CORE) normal-year atmosphere based on atmospheric reanalysis from 1958-2000 [*Large and Yeager*, 2004; *Griffies et al.*, 2009; *Small et al.*, 2015; *Whitt et al.*, 2019a]. The normal-year atmosphere is modified to approximate the conditions in 2100 by adding the monthly anomaly (2100 - 2000) of each forcing field (shortwave radiation, wind, surface air temperature etc) from the ensemble-mean annual cycle in the CESM large ensemble (CESM-LE, Kay et al, 2015). The CESM-LE includes 42 simulations of the historical emissions scenario (1920–2005) and the high-emissions Representative Concentration Pathway 8.5 (2006–2100) that differ from each other because very small random perturbations ($\mathcal{O}(10^{-14})$ K) are introduced to air temperature fields in 1920 [*Kay et al.*, 2015]. The ensemble mean anomalies represent the forced response of the climate system, averaging out natural modes of variability.

First, two branches are made from February 1 of year 21 of the control simulation of *Whitt et al.* [2019a], which is a global nominal-0.1° resolution mesoscale-resolving configuration of the Parallel Ocean Program (POP2) [*Smith et al.*, 2010] coupled to the

Community Ice Code version 5 [*Bailey et al.*, 2018] forced by the repeating normal-year atmosphere. The present-day branch is simply continued for 10 years without modifying the configuration. In the future-climate branch, the CESM-LE ensemble mean ocean temperature and salinity anomalies (2100 minus 2000) are added to the initial condition and then integrated forward with the constructed "future-climate" normal-year atmospheric forcing.

Submesoscale-permitting regional ocean simulations are obtained via nesting a high-resolution regional model within the global 0.1° model. The present-day and future-climate regional ocean simulations are conducted with the Regional Ocean Modeling System (ROMS) [*Shchepetkin and McWilliams*, 2005; *Haidvogel et al.*, 2008]; these simulations are the focus of this paper. ROMS was integrated on a nominally 0.01° (1.25 km) grid with 180 vertical sigma levels that are spaced using functions (2.2) and (2.4) of *Shchepetkin and McWilliams* [2009] and the stretching parameters $\theta_s = 7$, $\theta_b = 2$ and $h_c = 250$ m. The resulting vertical resolution is about 1.3 m at the surface and about 7.5 m at 250 m depth, and 43% of the grid levels are above 250 m. Lateral dissipation is done through a biharmonic hyperviscosity and hyperdiffusion with coefficients 3.3×10^6 m^{4}s^{-1} and 3.7×10^5 m^{4}s^{-1}, respectively.

The horizontal grid marginally resolves the fastest growing MLI wavelength, which is 2-3 km in summer and 10-12 km (4-6 km) in present-day (future) winter. This wavelength is estimated here by $L_{MLI} = (2\pi|\nabla_h b|H/f^2)\sqrt{(1+Ri_b^B)/(5/2)}$ [*Stone*, 1966], where the balanced bulk Richardson number $Ri_b^B = \Delta b f^2/(|\nabla_h b|^2 H)$, H is the mixed layer depth based on a change in density from the surface of $\Delta\rho = 0.03$ kg/m^3 and $\Delta b = g\Delta\rho/\rho_0$; all of the variables in L_{MLI} are smoothed to mesoscales by applying a 5-point square spatial

smoother 8 times [e.g., as in *Capet et al.*, 2008] to instantaneous snapshots (the filter damps the amplitude of a wave with wavelength of 30km by approximately 60%).

The bottom depth is based on ETOPO2 bathymetry [*National Geophysical Data Center, NOAA*, 2006], which is then limited to a range of 5000 m to 1200 m and smoothed to mitigate numerical issues following *Beckmann and Haidvogel* [1993]. The lateral boundary conditions are linearly interpolated from daily output of the analogous global 0.1° POP simulations using radiation and nudging constraints. Finally, ocean surface boundary layer dynamics are governed by the K-profile parameterization (KPP) of *Large et al.* [1994] with parameters as in the public ROMS repository at myroms.org. A diurnal cycle in solar radiation is imposed using analytic functions such that the daily mean solar radiation matches the normal year, and solar radiation penetrates using Jerlov type IB parameters [*Paulson and Simpson*, 1977].

Two additional runs are performed at a nominal 4km resolution, and vertical grid spacing twice that of the 1.25km runs. The lateral mixing coefficients are increased to be in line with those used in the POP runs with the damping affecting scales with a wavelength less than a nominal 60km. Specifically the biharmonic hyperviscosity and hyperdiffusion coefficients are set to 1.728×10^{10} m^4s^{-1} and 1.92×10^{9} m^4s^{-1}, respectively. Submesoscale motions are suppressed although, as seen below, not entirely eliminated. These runs will be referred to as "high viscosity"runs.

Each regional simulation is integrated for 3.3 years; this duration is chosen based on analysis of the 0.1° POP runs, which suggests there is little to gain from further integration since the adjustment process to the initial condition shock in the future-climate scenario is relatively slow after 3 years. Output for the whole integration period includes snapshots of

model variables every 5 days together with 12 hour averages. To consider higher frequency variability, snapshots every 3 hours were output for a 30-day period.

2.2. Study region

For the study here we consider a region in the North East Atlantic between 41°-51°N and 26°-13°W, which covers a region of deep ocean from the Porcupine Seabight (in the northeast) to the eastern flank of the Mid-Atlantic Ridge near the Azores (in the southwest). This region was chosen for a number of reasons. At the eastern edge of the North Atlantic subtropical gyre the mean flow is relatively weak and the mesoscale kinetic energy moderate, the depth of the mixed layer undergoes a large seasonal cycle (roughly 30–300m depth) and there is an observed seasonal cycle in submesoscale activity [*Thompson et al.*, 2016]. In addition, it is a region where large changes in the winter mixed layer depth and stratification are projected to occur under global warming caused in part by a surface freshening from Arctic ice melt [c.f. *Capotondi et al.*, 2012].

3. Results

The runs of the regional model at 1.25km resolution for the present–climate and future scenarios are labeled Run 2000 and Run 2100, respectively. The equivalent for the high viscosity runs are labeled Run2000visc and Run 2100visc. A key feature of the upper ocean is the depth to which properties are mixed from the surface. Various measures of this depth have been considered. Here the mixed layer depth (MLD) is taken as the depth H at which the change in density from the surface equals $\Delta\rho = 0.03$ kg/m^3.

Snapshots of H taken at 00:00 UTC (23:00 local time) on Feb. 15 are shown in Fig 1 for the various runs in the last year of integration. In the present-climate there is

considerable variation in H across the domain, with the shallow layers towards the west impacted by the presence of fresher surface waters. There is a damping of the finer scales in the high viscosity run. The large variation in H is reflected in the broad spread of the probability distribution function (pdf) of layer depths with a reduction in the number of occurrences of deeper values in the higher resolution run (Run 2000) compared with the high viscosity run (Run 2000visc). In the future climate there is an overall reduction in H and a sharpening of the pdf of H, although it is notable that there is an increase in the number of occasions of shallower H in the high viscosity run (Run 2100visc).

The domain averaged MLD, $< H >$, and lateral buoyancy gradient $< |\nabla_h b| >$ within the mixed layer are shown as a function of time in Fig. 2 for Runs 2000 and 2100. Day 0 here is Feb 1. In anticipation of examining the scaling for submesoscale activity following FFH, quantities have been spatially smoothed to the mesoscale (i.e., 8 applications of a 5-grid-point square window following *Capet et al.* [2008]). This does not affect $< H >$ but it does affect the quantiles of H. The depth of winter mixing is reduced in Run 2100 compared to Run 2000 (by a factor of more than 2 in the fourth winter of integration) with little change in the summer months.

For comparison the results for the high viscosity runs are shown. In the present–day climate the deepest winter time $< H >$ in Run 2000 is $\sim$20% less than in Run 2000visc, suggesting a restratification by the more active submesoscale activity in the former. There is little change between the runs in the summer. In contrast, comparing Runs 2100 and 2100visc, in the future climate state there is much less difference in $< H >$ throughout the year, with the notable exception of the fourth winter where $< H >$ is $\sim$20% deeper

in Run 2100 compared with the high viscosity run Run 2100visc (the snapshots shown in Fig. 1 are from this winter).

There is a strong seasonal cycle in the mean lateral buoyancy gradient, $< |\nabla_h b| >$, with its magnitude anti-correlated with the MLD in both climate states, i.e. the lateral buoyancy gradient is at a minimum during the deep winter mixing (Fig. 2). The mean lateral buoyancy gradient is not overly sensitive to the level of smoothing. Reducing the smoothing scale by applying 4 applications of the 5-grid-point square window (now a wave with wavelength of 20km is damped by approximately 60%) increases the mean gradient by less than 20%.. The seasonality in the lateral buoyancy gradient is similar in both phase and amplitude to that found by *Brannigan et al.* [2015] who suggest frontogensis strengthens gradients in the summer months while overturning instabilities, when the mixed layer is deep, weaken them in winter. There is notable interannual variability in both the mean MLD and lateral buoyancy gradient, the cause of which is not totally clear, although we note the long term decrease with time of $< |\nabla_h b| >$ in Run 2100 is associated with a reduction in the KE (which is not apparent in Run 2000). We will make use of this interannual variability when we come to consider the scaling of submesoscale activity in Section 3.2.

3.1. Spectra

Horizontal wavenumber spectra of velocity (Fig. 3) reveal how the kinetic energy (KE) is decomposed by horizontal scale and, in particular, isolates the submesoscale activity from activity at other scales in both the 2000 and 2100 runs. Fields are averaged over 36 hours and a linear trend is removed from each column and row before the spectra are calculated. The time series of horizontal and vertical KE spectra are at a depth of 100 m

for Run 2000 (Figs. 3a and b) and 50m for Run 2100 (Figs. 3d and e), the depths chosen to coincide with the depth of the peaks in vertical KE spectral energy (Figs. 3c and f). There is a strong seasonal cycle in the vertical KE spectral energy, peaking in January to March at a horizontal wavelength centered on ∼10km and restricted to depths close to the MLD. There is a clear separation between horizontal scales in the mixed layer, O(10km), the submesoscale, with those at depth, O(100km), the mesoscale. Near the surface there is a seasonal cycle in the slope with respect to wavenumber at shorter scales (shallower in winter than summer: see Fig. 4), with the seasonality dropping off with depth.

The horizontal KE spectral energy peaks at a wavelength of ∼200km. There is a reduction in energy at the mesoscale in the future run. Averaging the horizontal KE over wavenumber bands equivalent to 100-300km wavelength and from the surface to 100m depth the mesoscale KE reduces from 7.0×10^{-3} m^{2}s^{-2} to 3.6×10^{-3} m^{2}s^{-2} in the 2000 and 2100 runs respectively, a 49% reduction.

The spectra for the viscous runs 2000visc and 2100visc are shown in Figure 5. As expected there is a reduction in submesoscale activity, as seen in the vertical KE spectra, although it is not entirely eliminated. The submesoscale activity again peaks in the mixed layer and is reduced in amplitude in the future run, although at somewhat larger horizontal scale compared with the 2000 and 2100 runs. The average mesoscale KE is 2.4 $\times 10^{-3}$ m^{2}s^{-2} and 1.8×10^{-3} m^{2}s^{-2} in the 2000visc and 2100visc runs respectively, giving reduced values when compared to Runs 2000 and 2100, but also a smaller reduction, 26%, in going from the present to future states. There is a similar reduction, 22%, in the KE of the surface flow in the region found in the present and future runs of the 0.1 degree POP model. (The elevated bands of power in the vertical KE spectra at high wavenumber,

seen in Figs 5c and f, are presumed to come from the flow over the topography being inadequately resolved on the 4km grid. Their presence does not appear to impinge unduly on the near-surface submesoscale.)

The above spectral patterns are consistent with previous studies on submesoscale activity [e.g *Sasaki et al.*, 2014; *Callies et al.*, 2015]. What we show here is that a substantial change in submesoscale activity can occur under environmental change such as global warming. There is a large reduction in that activity in the future-climate scenario (Run 2100) compared with the present (Run 2000) with a reduction in depth over which it occurs, associated with the reduced MLD.

We also note that there is a larger reduction in the mesoscale KE going from the present to future climate state (49% Runs 2000 and 2100, respectively) compared with when the submesocale is suppressed (26%: Runs 2000visc and 2100visc, respectively). Differences in the mesoscale KE between runs are consistent with changes in the upscale transfer of energy from the submesoscale to mesoscale: higher submesoscale activity leading to higher rates of transfer. What we do not see, however, is a noticeable seasonal variation in the mesoscale KE associated with the seasonal variation in submesoscale activity, as seen in other studies such as *Dong et al.* [2020].

3.2. Vertical buoyancy flux

An important property of submesoscale activity is the enhancement of the vertical buoyancy flux. The vertical profile of the areal average vertical buoyancy flux, $< w'b' >$, on Feb 15 Year 4 is shown in Fig. 6a for Runs 2000 and 2100. Again, 36-hour averages of w and b are used to compute the flux, prime indicates the areal mean and linear trend in both horizontal directions have been subtracted from the variable, and $< \cdot >$ the

areal mean over the ROMS domain, excluding a 150km strip around the boundary. An indication of the spatial variability is given in Fig. 6a by the 0.2 and 0.8 quantile values (indicated by the shading).

Spatial variability of $w'b'$ on Feb. 15 Year 4 is shown in Figs. 7a and d for Runs 2000 and 2100 at a depth of 100m and 50m, respectively (approximately the middle of the mean mixed layer depth at this time in each run). The regions of high flux tend to be spatially confined and filamentary in nature (particularly for Run 2100) with the density of such features significantly higher in Run 2000 compared with Run 2100. Positive fluxes tend to be higher in amplitude than negative fluxes (as reflected in the quantiles shown in Fig 6a) with the areal mean flux being 15.5×10^{-9} and 9.5×10^{-9} $\mathrm{m^2 s^{-3}}$, respectively. Figs. 7b and e show the result of applying the spatial filter described above to smooth to the mesoscale for Runs 2000 and 2100, respectively. Although negative fluxes remain their contribution to the mean is much reduced.

The mean buoyancy flux, $< w'b' >$, peaks within the mixed layer (somewhat above the middle of the mean mixed layer for Run 2000), and is sharply reduced below the mean mixed layer depth, for both Runs 2000 and 2100 (Fig. 6a). The vertical structure indicates a tendency for the density to decrease in the upper part of the mixed layer and increase in the lower, i.e. a tendency, in the mean, for overturning within the mixed layer and restratification. The maximum $< w'b' >$ for Run 2000 is equivalent to a heat flux, Q_E, of $\sim$40 $\mathrm{Wm^{-2}}$ (which is within the 20-100 $\mathrm{W/m^2}$ range that is globally representative of mid-latitudes in *Su et al.* [2018]), where $Q_E = C_p \rho < w'b' > /(g\alpha_T)$ with C_p the specific heat and α_T the thermal expansion coefficient. The maximum buoyancy flux, and thus Q_E, is reduced by a factor of approximately 2 in Run 2100.

The maximum $< w'b' >$ within the mean mixed layer is shown in Fig. 6b as a function of time. The time interval, Days 600-1200, covers the winters of Years 3 and 4 (see Fig. 2). There is a strong seasonal cycle. For both Runs 2000 and 2100 the max. $< w'b' >$ is relatively small in spring and summer (AMJJA), increasing through the fall and early winter (SOND). The max. $< w'b' >$ is somewhat smaller for Run 2100 compared to Run 2000 in spring and summer but the largest difference occurs in late winter (JFM). For Run 2000 the max. $< w'b' >$ continues to rise, peaking in February, while it is relatively constant for Run 2100, the difference in peak value being approximately a factor of 2.

Much of the variation in max. $< w'b' >$ is consistent with variations in the mean mixed layer depth (Fig. 2a). The largest differences between Runs 2000 and 2100 occur in late winter (JFM) for both the buoyancy flux and mixed layer, when the later is at its deepest. There are, however, inconsistencies. Despite the deeper mixed layer depth in Year 4 compared to Year 3 of Run 2000, the peak in the buoyancy flux is approximately the same (Fig. 6b). In addition, the buoyancy flux in Run 2100 remains relatively flat during DJFM whereas the mixed layer is deepest in February (albeit at a shallower value than Run 2000).

For more insight into the factors controlling the buoyancy flux we turn to the scaling suggested by FFH. Using the properties of MLIs they suggest the buoyancy flux scales as $c < H^2|\nabla_h b|^2/|f| >$, where c is a scaling coefficient and H and $|\nabla_h b|$ are both smoothed to remove submesoscales before averaging (as in L_{MLI}). From idealized experiments of an unstable front they find that c lies in the range $c = 0.06 - 0.08$. The areal average of the FFH scaling is compared with the max. $< w'b' >$ in Fig. 6b with c=0.08 and quantities calculated as described above.

The areal mean of the FFH scaling captures well the seasonal behavior seen in max. $< w'b' >$ for both Run 2000 and 2100 (Fig. 6b), the former with a peak in late winter, the latter without. Even individual peaks on a monthly timescale are captured. A reduction in max. $< w'b' >$ between Run 2000 and 2100 in late winter is also present in the FFH scaling, although with the same scaling coefficient, c, the FFH scaling over predicts the reduction. FFH suggest a vertical structure function for the overturning streamfunction (μ(z) in their notation) that peaks in the middle of the mixed layer. The vertical position of max. $< w'b' >$ tends to be around 0.5 of the MLD in September decreasing to 0.3 and 0.4 of the MLD in February for Run 2000 and 2100, respectively.

The under-prediction of max. $< w'b' >$ by FFH when the areal mean MLD is relatively shallow may reflect the significance of other drivers of submesoscale vertical fluxes and restratification in shallow mixed layers [e.g., *Thomas*, 2005; *Long et al.*, 2012; *Whitt and Taylor*, 2017; *Whitt et al.*, 2019b]. The ratio, c^*, of the areal means $< w'b' >$ and $< H^2|\nabla_h b|/|f| >$ plotted as a function of the areal averaged mixed layer depth , $< H >$, is shown in Figure 8 for values from Days 600-1200 (the period shown in Fig. 6b). Effectively, c^* is the scaling constant of the FFH scaling when fitted to the model results for a given value of $< H >$. For 2100 and large $< H >$, $c^* \simeq 0.08$, the value of c used in comparison of the FFH scaling and model results shown in Fig. 6. For smaller values of $< H >$ there is an indication that the ratio (i.e. the scaling constant c) varies inversely with the areal mean MLD. For Run 2100 there is a similar increase in the ratio for decreasing $< H >$ for small $< H >$, but is more constant for $< H >$ between 50-100m at a value approximately twice that of the asymptotic value for Run 2000.

Again there is considerable spatial variability (see Figs. 7c and f for Runs 2000 and 2100, respectively) with high values of the FFH scaling tracing out the areas of high amplitude buoyancy flux (Fig. 7a and c, respectively), particularly evident in Run 2100. This is also true for the spatially smoothed buoyancy flux (Fig. 7b and e), although we have not investigated the optimal smoothing for such a comparison. The comparison is somewhat better for the sparser structures seen in Run 2100. The areal mean of the FFH scaling (with c=0.08) is 16.4×10^{-9} m^{2}s^{-3} and 4.8×10^{-9} m^{2}s^{-3} for Runs 2000 and 2100, respectively, the latter being approximately half the mean of $< w'b' >$ at 50m. This is consistent with the results shown in Fig. 8 (noting that max. $< w'b' >$ is used in the ratio c^* rather than the flux at a given depth).

The spatial variability in the FFH scaling is primarily caused by the spatial variability in $|\nabla_h b|$ rather than H. The variables contributing to the FFH scaling are compared in (Fig. 9). The spatial variability of $|\nabla_h b|$ (Fig. 9b) corresponds very well to that of the FFH scaling (Fig. 9a), whereas there is less correspondence of the high values of H (Fig. 9d) with the high values of the FFH scaling. Indeed there is a tendency for H to be *shallower* in regions where the scaling is *high* indicating either the choice of definition of the MLD picks out the frontal regions or the scaling is showing regions of restratification induced by submesoscale processes. Given the dominance of $|\nabla_h b|$, Figure 9b shows the FFH scaling with H^2 replaced by $< H >^2$, labeled FFH$_o$. The correspondence of FFH$_o$ with the original FFH scaling (Figure 9a) is very good. FFH$_o$ tends to over estimate FFH, again reflecting the tendency for H to be shallower in regions of high $|\nabla_h b|$.

Returning to the inconsistencies between variations of the buoyancy flux and the mixed layer depth alone, we see they can be resolved by including variations in the lateral

buoyancy gradient with reference to the FFH scaling. The increase in the winter MLD, H, in Year 4 compared to Year 3 (Fig. 2) is compensated by a decrease in the winter time $|\nabla_h b|$, resulting in little change in the buoyancy flux. In fact the FFH scaling over compensates (Fig. 6b). In Run 2100 the rate of decrease in $|\nabla_h b|$ in late winter is enough to compensate the rate of increase in H leading to the relatively flat variation with time in winter months.

Lastly, we have used 36 hourly averages of variables to compute the spectra and buoyancy flux. As shown by the modeling studies of *Torres et al.* [2018] and *Su et al.* [2020], however, there is considerable variability at higher frequencies. Observations also show submesoscale motions can have a relatively short time scale [*Callies et al.*, 2020]. Fig. 10 compares the max. $< w'b' >$ within the mixed layer calculated using 3-hour output compared to 36 hourly averages for a short (30 day) period at a time when the mixed layer is deep (see Fig. 2). There is a strong diurnal signal as well as a near-inertial signal in the flux calculated with the high frequency output (established from a Fourier transform of the time series), on top of the lower frequency variations found using the 36 hourly averages, that approximately doubles the flux averaged over the time period shown for both Run 2000 and 2100.

The spatial variability of $w'b'$ on Feb. 15 Year 4 using snapshot values of w' and b' is shown in Figs. 11a and b for Runs 2000 and 2100 at a depth of 100m and 50m, respectively. A spatial filter has been applied to smooth to the mesoscale. The spatial structure is similar to the result using 36-hour averages and the FFH scaling (Figs. 7b-c and e-f, respectively). The areal mean is 4.0×10^{-8} and 2.1×10^{-8} $\mathrm{m^2 s^{-3}}$, respectively, a little over twice the values using 36-hour averages.

To extend the period of comparison we have calculated the max. $< w'b' >$ from snapshots of w and b taken every 5 days throughout the integration period (see Fig. 12). The snapshots are taken at 00:00 UTC (23:00 local time) when the flux tends to be relatively high (but not always: see Fig. 10). In the winter months (deep mixed layer) the flux calculated from the 5-day snapshots tends to be greater than that calculated from 36 hour averages by a factor $\sim$2 for both Runs 2000 and 2100 (similar to that seen in Fig. 10 for the high frequency snapshots). In the summer months there is less consistency. For Run 2100 there is no noticeable difference in the flux using the 5-day snapshots and 36 hour averages, while for Run 2000 the 5-day snapshots do show periods when the flux is elevated.

4. Conclusions and discussion

In the context of the experiments reported here we find the imposed climate change impacts submesoscale activity. Associated with a reduced mixed layer depth in a warmer climate there is a marked reduction in vertical motions at the submesoscale (Fig. 3) together with a factor two decrease in the areal-mean vertical buoyancy flux in late winter (Fig. 6). Changes to the lateral buoyancy gradient also play a role. We have seen that changes in the mean mesoscale lateral buoyancy gradient, $< |\nabla_h b| >$, in successive winters can counter changes to the mean mixed layer depth, although in the case considered (Years 3 and 4) the variation in $< |\nabla_h b| >$ was very similar in the present and future runs (Fig. 2b). Longer simulations and examination of different regions are needed to establish the relative roles of future changes to mixed layer depth and lateral buoyancy gradients in affecting submesoscale activity.

To establish how the presence of submesoscale activity impacts the response to climate change, results are compared to runs with high lateral mixing coefficients to suppress (but not totally eliminate) submesoscale activity. In these runs where submesoscale activity was suppressed, climate change generated larger reductions in winter mixed layer depths than in the submesoscale permitting integrations. The change at the mesoscale is also affected by the presence of submesoscale activity through changes to the non-linear energy exchanges between mesoscales and submesoscales. The reduction in mesoscale KE going from the present to future climate states (Runs 2000 and 2100) at 49% is much greater than the reduction when the submesoscale is suppressed (Runs 2000visc and 2100visc) at 26%.

The scaling for the vertical buoyancy flux suggested by FFH, namely $cH^2|\nabla_h b|^2/|f|$, captures much of the seasonal and future changes to the areal mean flux (Fig. 6b). The scaling offers a promising way forward in terms of parameterizing the impact of submesoscale activity. There are differences, however, and clearly the scaling does not capture all factors affecting changes to the vertical buoyancy flux, in particular when the MLD is relatively shallow or in the more stratified state in the future climate (see Fig. 8). More numerical experimentation is needed to elucidate why these differences occur.

There are issues with regard to how well the grid resolution of the model runs resolves the submesoscale activity, as with all such studies [see e.g. *Brannigan et al.*, 2015], and in particular the changes to that activity under environmental change. Our conclusions need to be be tested by establishing the sensitivity to the horizontal and vertical resolutions as well as the explicit diffusivities. Here we can report that additional runs with the coarser grid ($\sim$4km) but with lower biharmonic lateral mixing coefficients, which lie between the

high-viscosity and 1.25 km cases, show a similar factor 2 reduction in the vertical buoyancy fluxes in winter months as seen with the higher resolution ∼1.25km grid. With a grid spacing of ∼1.25km the model is not fully resolving the expected scales of MLI in the summer months. The results in the summer months need to be treated with caution, in particular with regard to changes, or lack thereof, from the present day to future climate states. We note, however, the vertical buoyancy fluxes when the mixed layer is relatively shallow are significantly greater than those given by the FFH scaling (if a constant scaling coefficient is used: Fig. 8). Thus, other processes (besides MLI) that may be resolved on the 1.25 km grid may dominate submesoscale buoyancy fluxes during summer.

We stress the need to consider the lateral structure of the flow as well as areal means. Here we note the localized nature of the impact of submesoscale activity and the decrease in density of high flux regions within the domain going from the present to future climate states (see Fig. 7). This localization will impact the biogeochemistry as well as the physics and needs to be considered when the submesoscale processes are parameterized. The dominance of the lateral buoyancy gradient in the FFH scaling at these small scales suggests that an effective estimate of the FFH scaling may be obtained from combining satellite measurements (to get an estimate of the lateral buoyancy gradient) and coarser *in situ* measurements (for MLD).

Lastly, we have noted the large impact of including diurnal and near-inertial variations in the calculation of the vertical buoyancy flux. There appears to be a consistent factor ∼2 increase in winter months in the flux compared with when using 36-hourly averaged values that filter out these high frequency variations for both the present-day and future climate states. There is less consistency in the summer months. Additional analysis

and experimentation is needed to elucidate how quantities such as the vertical flux of buoyancy are impacted by the strength of the diurnal cycle and near-inertial motions and ocean state.

Acknowledgments. Datasets for this research are available at *Richards et al.* [2020a] and plotting scripts at *Richards et al.* [2020b].

This work is funded by the National Science Foundation (NSF) under grants OCE-1658550 and OCE-1658541. Discussions with Andrew Thompson on the experimental design and analysis of results are gratefully acknowledged. This material is based upon work supported by the National Center for Atmospheric Research, which is a major facility sponsored by the NSF under Cooperative Agreement No. 1852977. Computing and data storage resources, including the Cheyenne supercomputer (doi:10.5065/D6RX99HX), were provided by the Computational and Information Systems Laboratory (CISL) at NCAR. We thank all the scientists, software engineers, and administrators who contributed to the development of CESM. DBW also acknowledges support from the NSF, via OPP-1501993, NOAA, via NA18OAR4310408, and NASA, via 80NSSC19K1116.

References

Ascani, F., K. J. Richards, E. Firing, S. Grant, K. S. Johnson, Y. Jia, R. Lukas, and D. M. Karl (2013), Physical and biological controls of nitrate concentration in the upper North Pacific subtropical ocean, *Deep Sea Research II*, *93*, 119–134.

Bailey, D., A. DuVivier, M. Holland, E. Hunke, B. Lipscomb, B. Briegleb, C. Bitz, and J. Schramm (2018), CESM CICE5 Users Guide.

Beckmann, A., and D. B. Haidvogel (1993), Numerical simulation of flow around a tall isolated seamount. part i: Problem formulation and model accuracy, *Journal of physical oceanography*, *23*(8), 1736–1753.

Boccaletti, G., R. Ferrari, and B. Fox-Kemper (2007), Mixed layer instabilities and restratification, *J. Phys. Oceanogr.*, *37*(9), 2228–2250, doi:10.1175/JPO3101.1.

Brannigan, L., D. P. Marshall, A. Naveira-Garabato, and A. J. George Nurser (2015), The seasonal cycle of submesoscale flows, *Ocean Modelling*, *92*, 69–84, doi:10.1016/j.ocemod.2015.05.002.

Callies, J., R. Ferrari, J. M. Klymak, and J. Gula (2015), Seasonality in submesoscale turbulence, *Nature Communications*, *6*, 6862, doi:10.1038/ncomms7862.

Callies, J., G. Flierl, R. Ferrari, and B. Fox-Kemper (2016), The role of mixed-layer instabilities in submesoscale turbulence, *Journal of Fluid Mechanics*, *788*, 5–41.

Callies, J., R. Barkan, and A. Naveira Garabato (2020), Time scales of submesoscale flow inferred from a mooring array, *Journal of Physical Oceanography*, *50*(4), 1065–1086, doi:10.1175/JPO-D-19-0254.1.

Capet, X., J. C. McWilliams, M. J. Molemaker, and A. F. Shchepetkin (2008), Mesoscale to Submesoscale Transition in the California Current System. Part I: Flow Structure, Eddy Flux, and Observational Tests, *J. Phys. Oceanogr.*, *38*, 29, doi:10.1175/2007JPO3671.1.

Capet, X., E. Campos, and A. Paiva (2008), Submesoscale activity over the argentinian shelf, *Geophysical Research Letters*, *35*(15).

Capotondi, A., M. A. Alexander, N. A. Bond, E. N. Curchitser, and J. D. Scott (2012), Enhanced upper ocean stratification with climate change in the CMIP3 models, *J.*

Geophys. Res., *117*, C04031, doi:10.1029/2011JC007409.

Dong, J., B. Fox-Kemper, H. Zhang, and C. Dong (2020), The seasonality of submesoscale energy production, content, and cascade, *Geophys. Res. Lett.*, *47*, doi:10.1029/2020GL087388.

Fox-Kemper, B., R. Ferrari, and R. Hallberg (2008), Parameterization of mixed layer eddies. Part I: Theory and diagnosis, *J. Phys. Oceanogr.*, *38*(6), 1145–1165, doi:10.1175/2007JPO3792.1.

Griffies, S. M., et al. (2009), Coordinated ocean-ice reference experiments (COREs), *Ocean Modelling*, *26*(1-2), 1–46.

Haidvogel, D. B., et al. (2008), Ocean forecasting in terrain-following coordinates: Formulation and skill assessment of the regional ocean modeling system, *Journal of Computational Physics*, *227*(7), 3595–3624.

Kay, J. E., et al. (2015), The community earth system model (CESM) large ensemble project: A community resource for studying climate change in the presence of internal climate variability, *Bulletin of the American Meteorological Society*, *96*(8), 1333–1349.

Klein, P., and G. Lapeyre (2009), The oceanic vertical pump induced by mesoscale and submesoscale turbulence, *Ann. Rev. of Mar. Sci.*, *1*(1), 351–375, doi:10.1146/annurev.marine.010908.163704.

Large, W. G., and S. G. Yeager (2004), Diurnal to decadal global forcing for ocean and sea-ice models: the data sets and flux climatologies, doi:10.5065/D6KK98Q6.

Large, W. G., J. C. McWilliams, and S. C. Doney (1994), Oceanic vertical mixing: a review and model with a nonlocal boundary layer parameterisation, *Reviews of Gephysics*, *32*, 363–403.

Lévy, M., P. Klein, and A.-M. Treguier (2001), Impact of sub-mesoscale physics on production and subduction of phytoplankton in an oligotrophic regime, *J. Mar. Res.*, *59*(4), 535–565, doi:10.1357/002224001762842181.

Lévy, M., R. Ferrari, P. J. S. Franks, A. P. Martin, and P. Rivière (2012), Bringing physics to life at the submesoscale, *Geophy. Res. Lett.*, *39*, L14602, doi:10.1029/2012GL052756.

Lévy, M., P. Franks, and K. Smith (2018), The role of submesoscale currents in structuring marine ecosystems, *Nature Communications*, *9*, 4758, doi: https://doi.org/10.1038/s41467-018-07059-3.

Long, M. C., L. N. Thomas, and R. B. Dunbar (2012), Control of phytoplankton bloom inception in the Ross Sea, Antarctica, by Ekman restratification, *Global Biogeochem. Cycles*, *26*(1), GB1006, doi:10.1029/2010GB003982.

Mahadevan, A. (2016), The impact of submesoscale physics on primary productivity of plankton, *Annual Review of Marine Science*, *8*, 161–184.

Mahadevan, A., E. D'Asaro, C. Lee, and M. J. Perry (2012), Eddy-Driven Stratification Initiates North Atlantic Spring Phytoplankton Blooms, *Science*, *337*, 54–58, doi: 10.1126/science.1218740.

McWilliams, J. (2016), Submesoscale currents in the ocean, *Proceedings of the Royal Society A: Mathematical, Physical and Engineering Sciences*, *472(2189)*, p.20160,117.

Mensa, J. A., Z. Garraffo, A. Griffa, T. M. Özgökmen, A. Haza, and M. Veneziani (2013), Seasonality of the submesoscale dynamics in the Gulf Stream region, *Ocean Dynamics*, *63*, 923–941, doi:10.1007/s10236-013-0633-1.

National Geophysical Data Center, NOAA (2006), 2-minute gridded global relief data (etopo2v2) doi:10.7289/V5J1012Q.

534 Paulson, C. A., and J. J. Simpson (1977), Irradiance measurements in the upper ocean,
535 *Journal of Physical Oceanography*, *7*(6), 952–956.

536 Richards, K., D. Whitt, and G. Brett (2020a), Climate change impact on submesoscale
537 ROMS data (data set), doi:10.5281/zenodo.3892107.

538 Richards, K., D. Whitt, and G. Brett (2020b), gjayb/submesoClimate: Initial release
539 (Version v1.0), doi:10.5281/zenodo.3895340.

540 Sasaki, H., P. Klein, B. Qiu, and Y. Sasai (2014), Impact of oceanic-scale interactions on
541 the seasonal modulation of ocean dynamics by the atmosphere, *Nature Communications*,
542 *5*, 5636, doi:10.1038/ncomms6636.

543 Shchepetkin, A. F., and J. C. McWilliams (2005), The regional ocean modeling system
544 (ROMS): a split-explicit, free-surface, topography-following coordinate oceanic model.,
545 *Ocean Model.*, *9*, 347–404.

546 Shchepetkin, A. F., and J. C. McWilliams (2009), Correction and commentary for "Ocean
547 forecasting in terrain-following coordinates: Formulation and skill assessment of the
548 regional ocean modeling system" by Haidvogel et al., J. Comp. Phys. 227, pp. 3595–
549 3624, *Journal of Computational Physics*, *228*(24), 8985–9000.

550 Small, R. J., E. Curchitser, K. Hedstrom, B. Kauffman, and W. G. Large (2015), The
551 benguela upwelling system: Quantifying the sensitivity to resolution and coastal wind
552 representation in a global climate model, *Journal of Climate*, *28*(23), 9409–9432.

553 Smith, R., et al. (2010), The parallel ocean program (POP) reference manual ocean com-
554 ponent of the community climate system model (CCSM) and community earth system
555 model (CESM), *Rep. LAUR-01853*, *141*, 1–140.

Stone, P. (1966), On non-geostrophic baroclinic stability, *Journal of the Atmospheris Sciences*, *23*(4), 390–400.

Su, Z., J. Wang, P. Klein, A. F. Thompson, and D. Menemenlis (2018), Ocean submesoscales as a key component of the global heat budget, *Nature Communications*, *9*(1), 1–8.

Su, Z., H. Torres, P. Klein, A. Thompson, L. Siegelman, J. Wang, D. Menemenlis, and C. Hill (2020), High-frequency submesoscale motions enhance the upward vertical heat transport in the global ocean, *J. Geophys. Res.*, *125*(9), doi:10.1029/2020JC016544.

Taylor, J. R., and R. Ferrari (2011), Ocean fronts trigger high latitude phytoplankton blooms, *Geophy. Res. Lett.*, *38*, L23601, doi:10.1029/2011GL049312.

Thomas, L. (2005), Destruction of potential vorticity by winds, *J. Phys. Oceanogr.*, *35*(12), 2457–2466.

Thompson, A., A. Lazar, C. Buckingham, A. Naveira Garabato, G. Damerell, and K. Heywood (2016), Open-ocean submesoscale motions: A full seasonal cycle of mixed layer instabilites from gliders., *J. Phys. Oceanogr.*, *46*, 1285–1307.

Torres, H., P. Klein, D. Menemenlis, B. Qiu, Z. Su, J. Wang, S. Chen, and L. Fu (2018), Partitioning ocean motions into balanced motions and internal gravity waves: A modeling study in anticipation of future space missions., *J. Geophys. Res.*, *123*, 8084–8105, doi:110.1029/2018JC014438.

Whitt, D. B., and J. R. Taylor (2017), Energetic submesoscales maintain strong mixed layer stratification during an autumn storm, *Journal of Physical Oceanography*, *47*(10), 2419–2427.

Whitt, D. B., S. A. Nicholson, and M. M. Carranza (2019a), Global impacts of subseasonal (< 60 day) wind variability on ocean surface stress, buoyancy flux, and mixed layer depth, *Journal of Geophysical Research: Oceans*, *124*(12), 8798–8831, doi: 10.1029/2019JC015166.

Whitt, D. B., M. Lévy, and J. R. Taylor (2019b), Submesoscales enhance storm-driven vertical mixing of nutrients: Insights from a biogeochemical large eddy simulation, *Journal of Geophysical Research: Oceans*, *124*(11), 8140–8165.

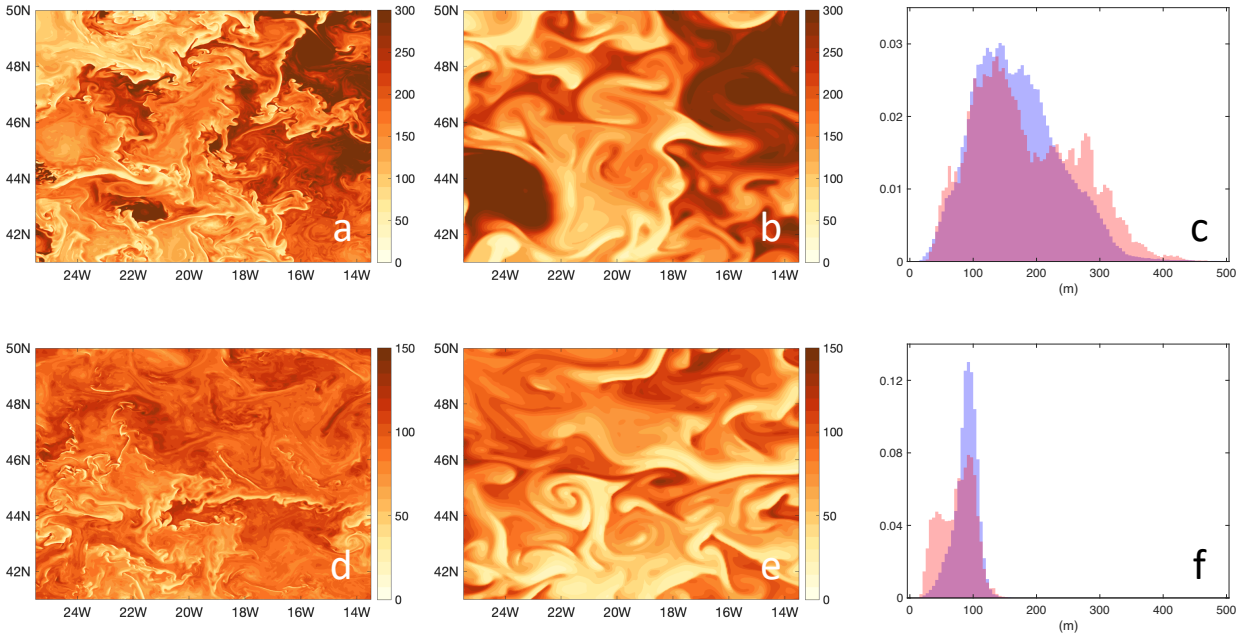

Figure 1. (a) depth of the mixed layer, H, on Feb. 15 in the present climate (Run 2000) over the ROMS domain. (b) the same as (a) but with high viscosity (Run 2000visc). (c) the pdf of the distribution of H in (a) and (b) (blue and red, respectively). (e-f) the same as (a-c) but for the future climate (Runs 2100 and Run 2100visc). Units: m.

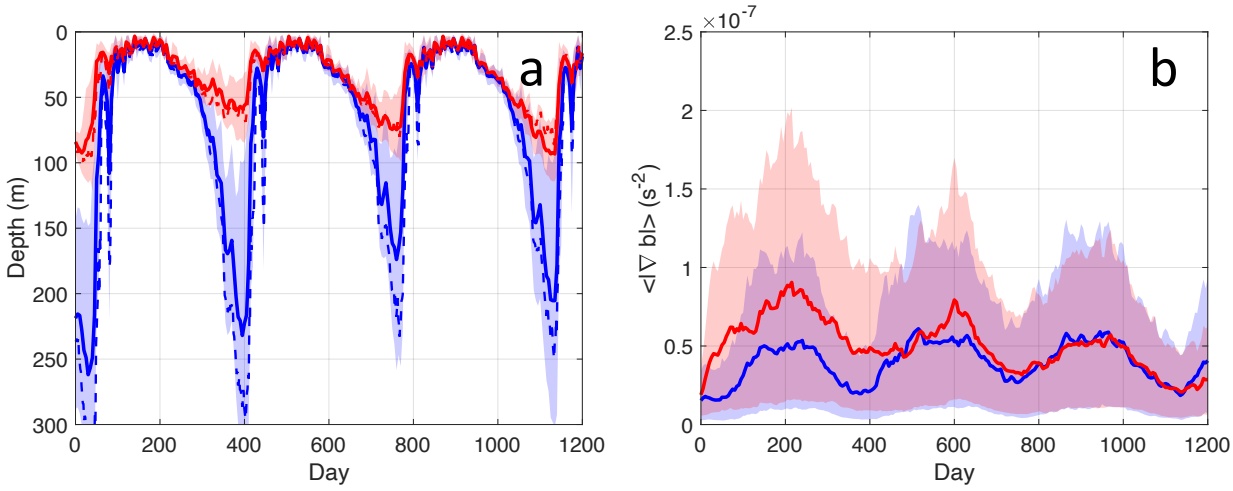

Figure 2. The areal average of (a) the mixed layer depth (based on the $\Delta\rho = 0.03$ kg/m^3 density threshold) and (b) the lateral buoyancy gradient as a function of time. Quantities are calculated from instantaneous snapshots of variables with a spatial filter applied to remove the smallest spatial scales (see text): solid blue line Run 2000, solid red line Run 2100. The shading indicates the interval between the 0.1 and 0.9 quantiles. In (a): dashed blue line Run 2000visc, dashed red line Run 2100visc. Day 0 is Feb. 1.

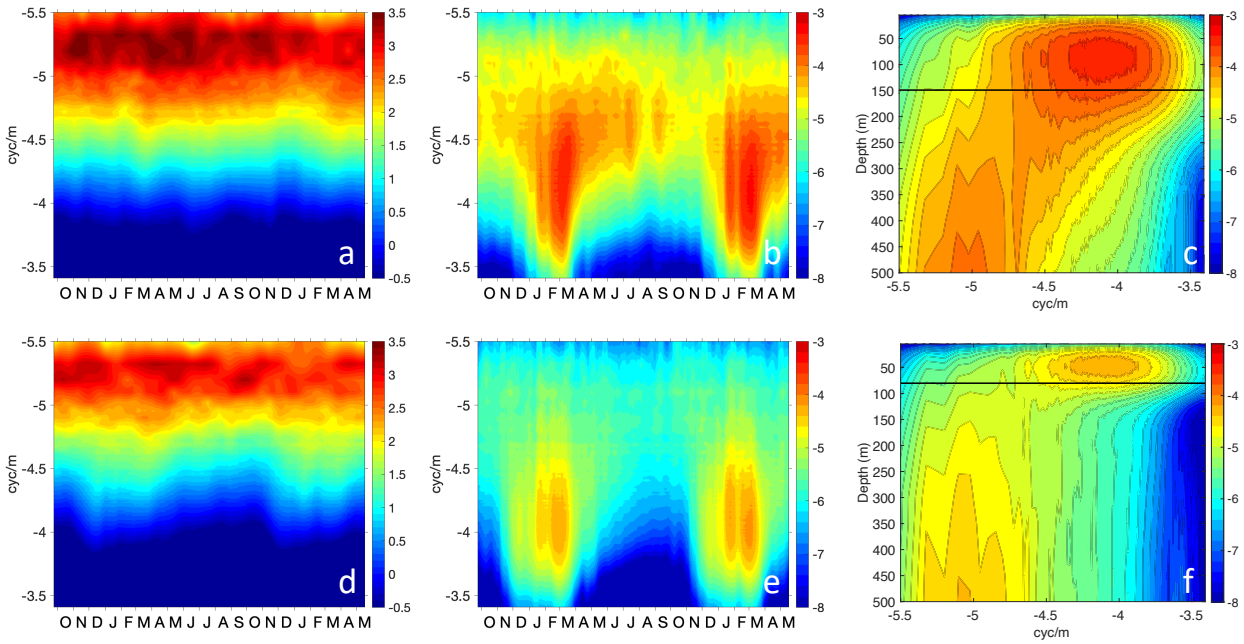

Figure 3. Radially-integrated velocity horizontal wavenumber spectra. (a) and (b) $\log_{10}$ horizontal and vertical kinetic energy power spectra for Run 2000, respectively, at a depth of 100m as a function of wavenumber (cycles/m) and time (Days 600-1200 with time indicated as month of the year). (c) $\log_{10}$ vertical kinetic energy power spectrum on Feb 15 Year 4 for Run 2000 as a function and depth and wavenumber. (d)-(f) same as (a)-(c) but for Run 2100, with (d) and (e) at a depth of 50m. Units m^2s^{-2} $(cyc/m)^{-1}$. Horizontal lines in (c) and (f) show the mean depth of the mixed layer. Fields are averaged over 36 hours and a linear trend is removed from each column and row before the spectra are calculated.

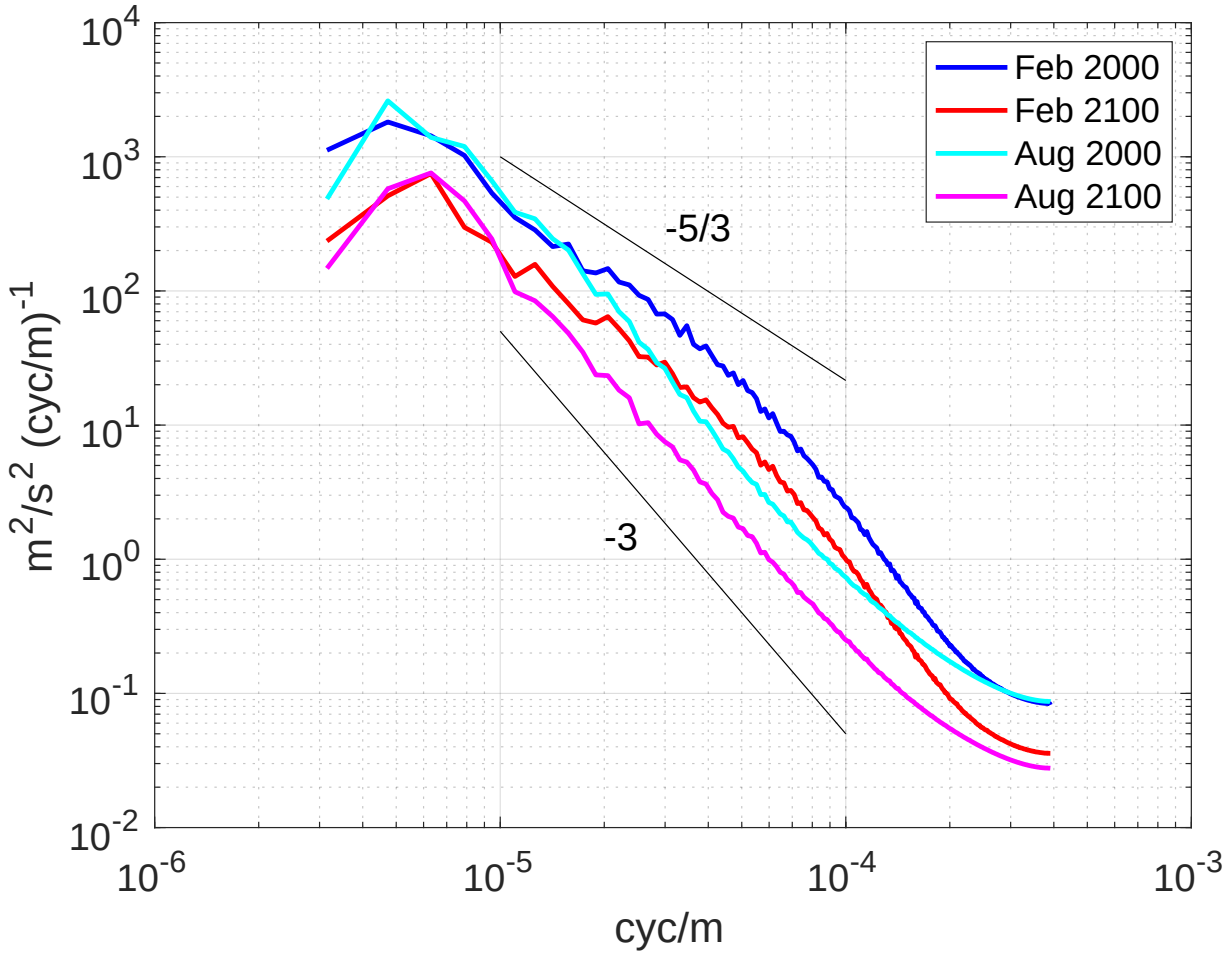

Figure 4. Horizontal wavenumber spectra of the horizontal kinetic energy at 20m depth averaged over the months of August (Year 3) and February (Year 4) for Runs 2000 and 2100.

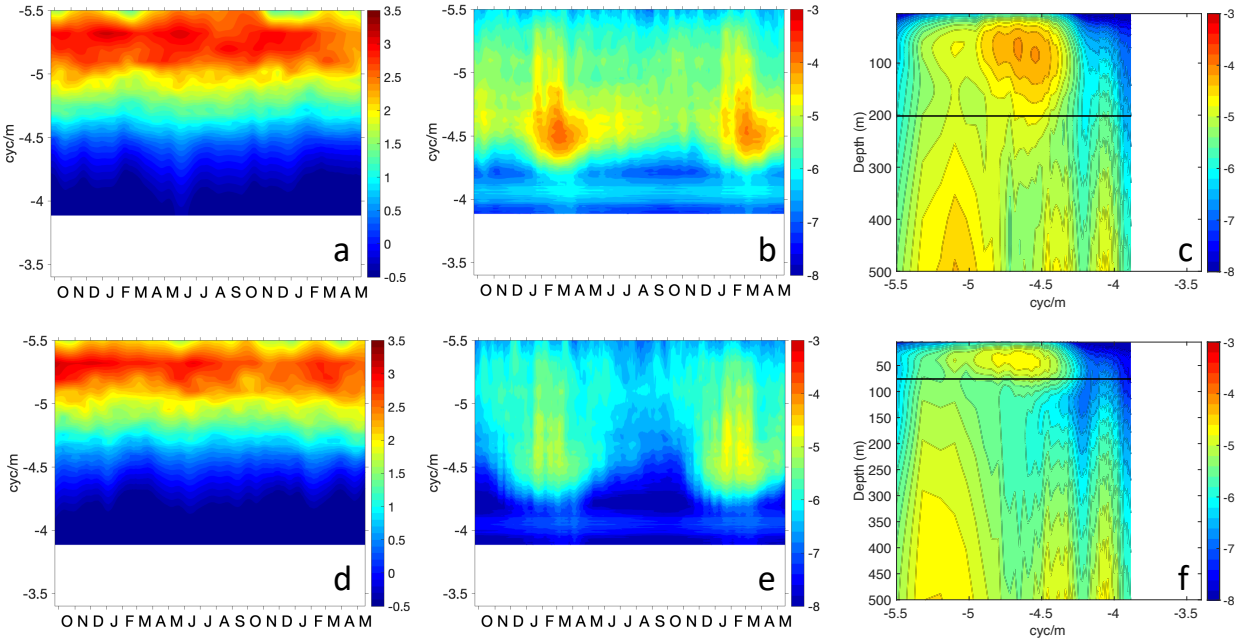

Figure 5. Same as Figure 3 but for Runs 2000visc and 2100visc.

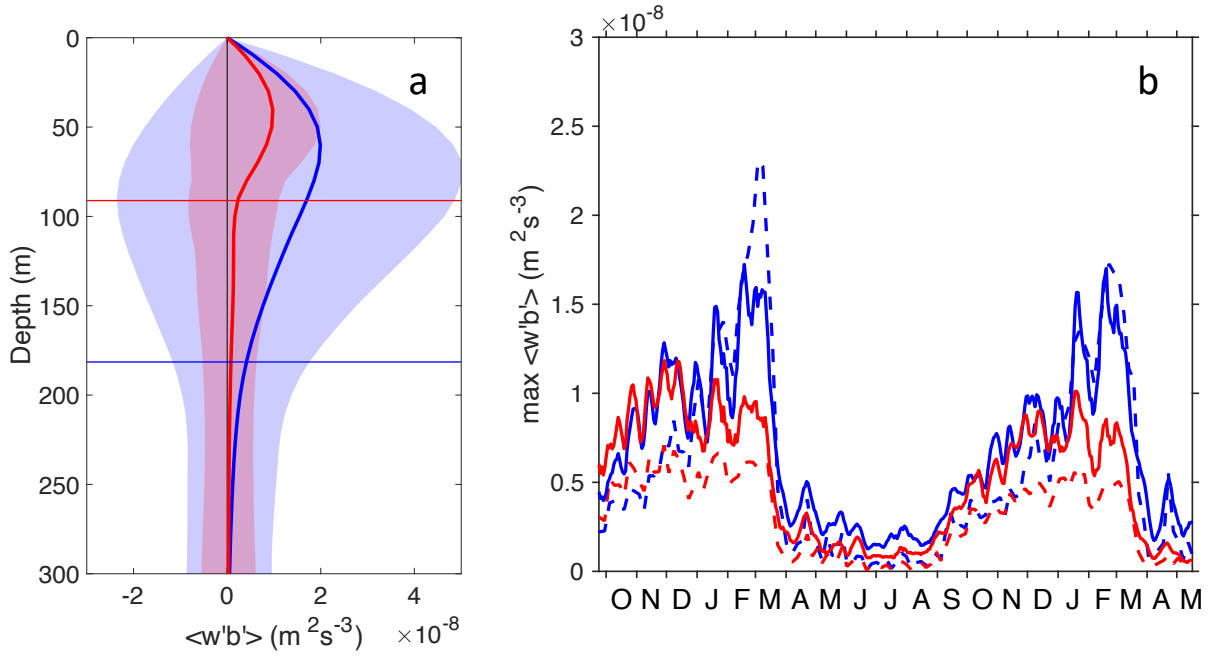

Figure 6. (a) The areal average vertical buoyancy flux $< w'b' >$ on Feb 15 Year 4 as a function of depth (the flux is calculated with 36 hour averages of variables): solid blue line Run 2000, solid red line Run 2100. Horizontal lines show the mean depth of the mixed layer for each run. The shading indicates the interval between the 0.2 and 0.8 quantiles. (b) The maximum $< w'b' >$ within the mixed layer as a function of time for Days 600-1200 (time is given as month of the year): solid blue line Run 2000, solid red line Run 2100. A 7-day running mean has been applied. Dashed lines are the FFH scaling for each run with the scaling coefficient c=0.08.

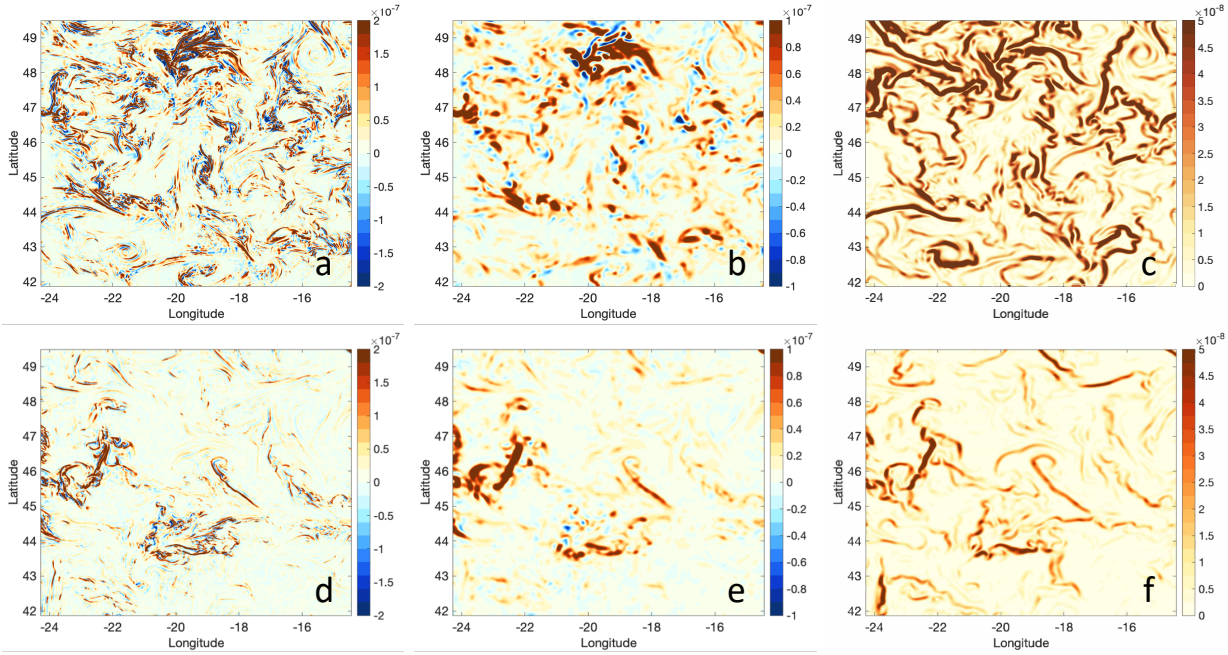

Figure 7. (a) Spatial variability of $w'b'$ for Run 2000 at a depth of 100m on Feb. 15 Year 4 (b) The same as (a) but with a spatial smoothing (smoothed to the mesoscale: see text) applied to the field. (c) The FFH scaling for Run 2000 on Feb. 15 Year 4. (d-f) same as (a-c) but at a depth of 50m for Run 2100. Units: m^2s^{-3} (note the color bars vary)

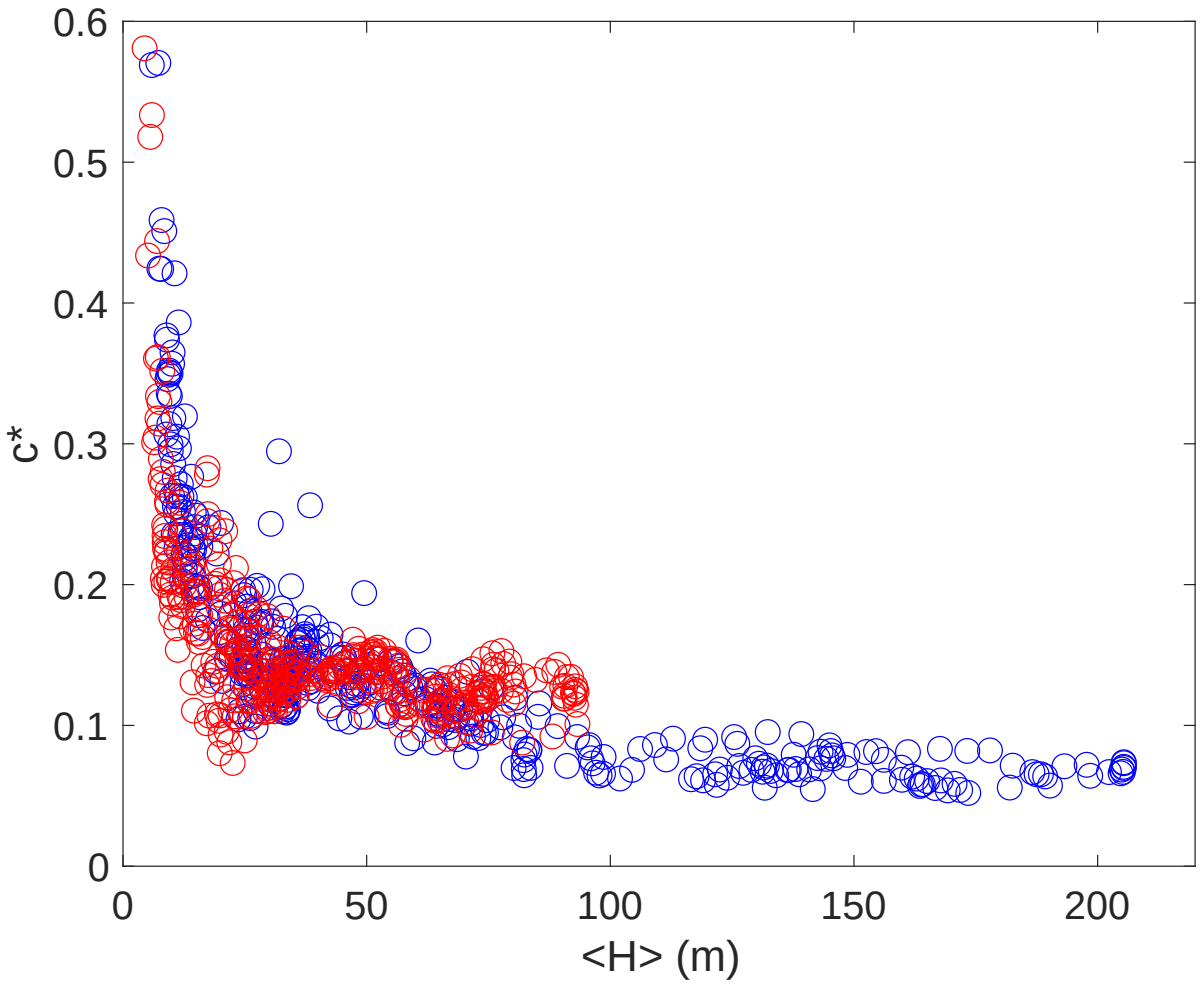

Figure 8. c^* ($=< w'b' > / < H^2|\nabla_h b|/|f| >$) plotted as a function of the areal average mixed layer depth, $< H >$, for values from Days 600-1200. Blue circles Run 2000. Red circles Run 2100.

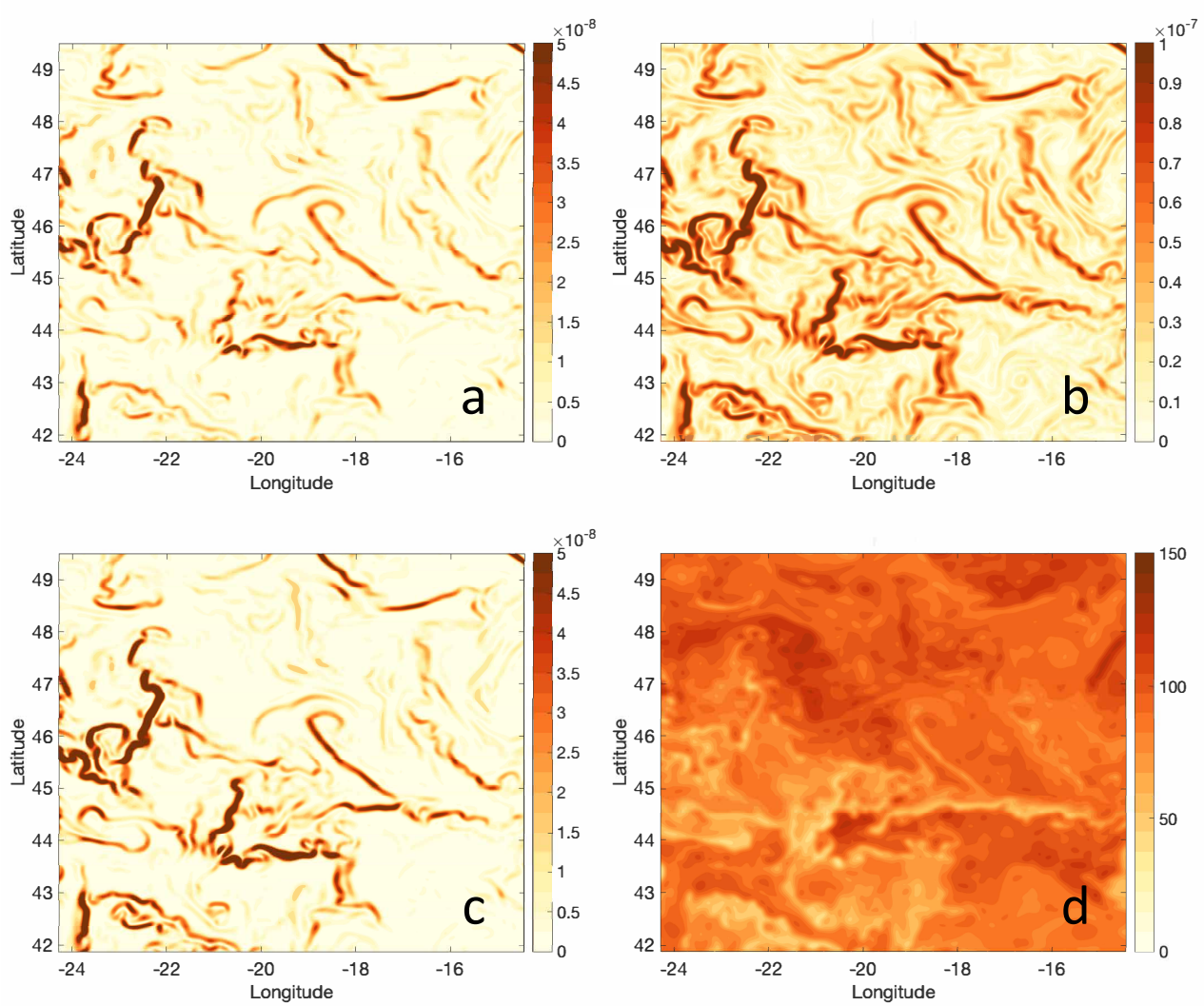

Figure 9. Contributions to the FFH scaling for Run 2100 on Feb. 15 Year 4. (a) FFH scaling (m^2s^{-3}) (b) $|\nabla_h b|$ (s^{-2}) (c) FFH_o: FFH scaling with H^2 replaced by $< H >^2$ (d) H.

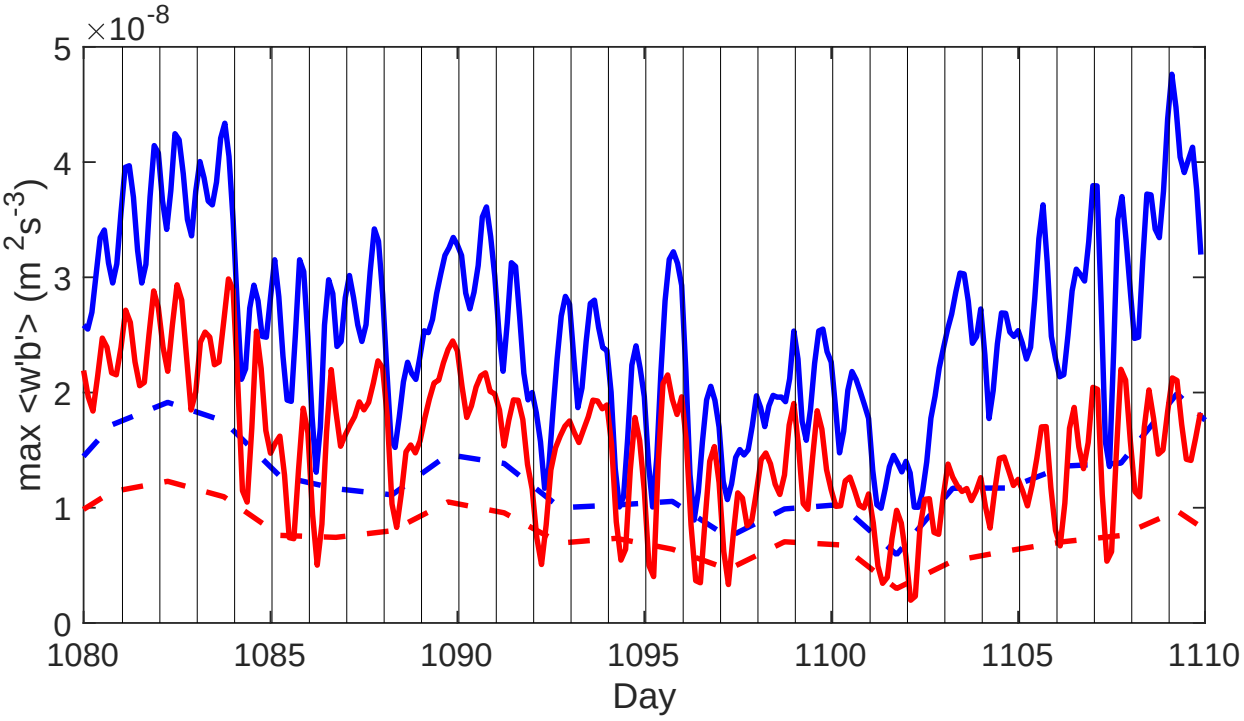

Figure 10. The maximum $< w'b' >$ within the mixed layer as a function of time comparing different temporal averaging of variables used in the flux calculation: solid lines high frequency (3 hourly) snapshots, dashed lines using 36 hour averaged values of variables, blue lines Run 2000, red lines Run 2100. Local midnight indicated by thin black lines.

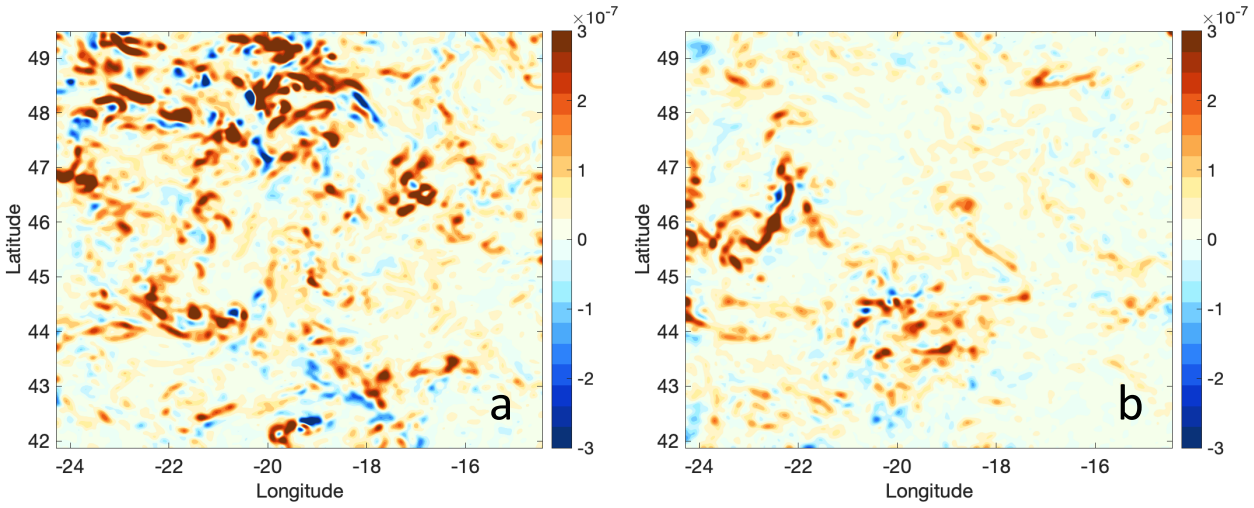

Figure 11. (a) Spatial variability of $w'b'$ calculated using snapshot values of w' and b' for Run 2000 at a depth of 100m on 12:00 local time Feb. 15 Year 4. A spatial smoothing (smoothed to the mesoscale: see text) has been applied to the field. (b) same as (a) but at a depth of 50m for Run2100. Units: m^2s^{-3}

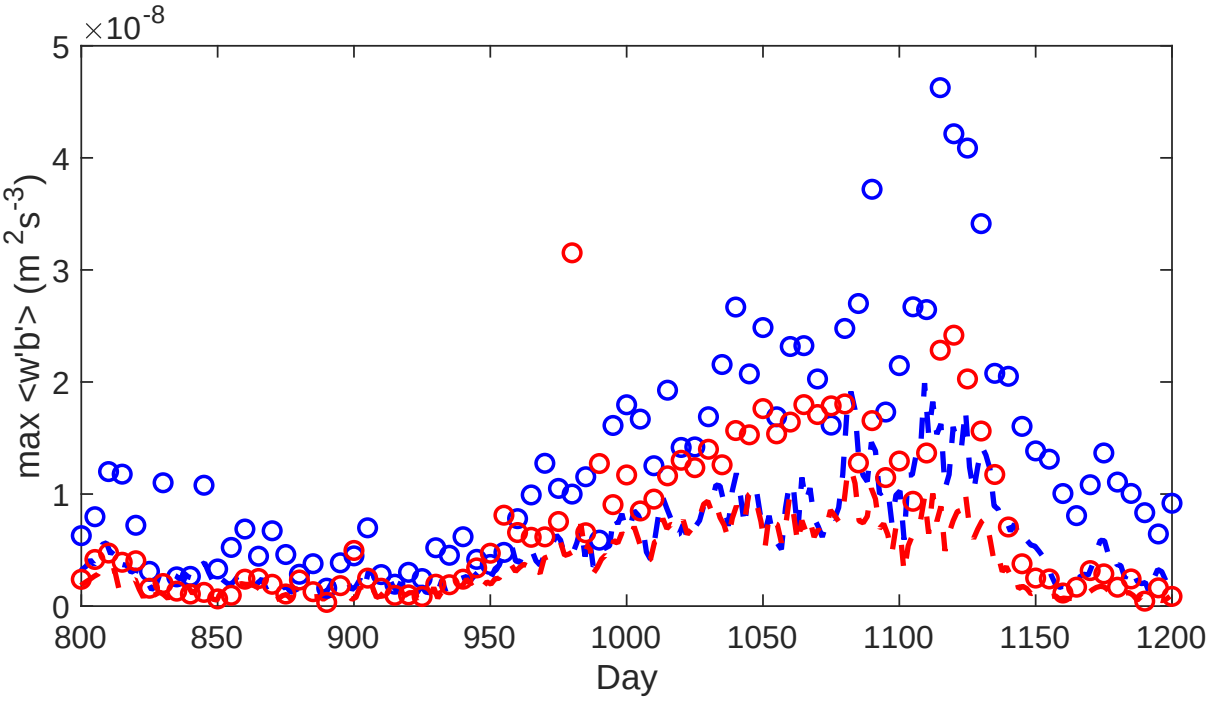

Figure 12. As Figure 10 but for snapshot values every 5 days (open circles) compared with 36 hour averaged values (dashed lines)